Original Article

# The chitosan-based bioactive composite coating on titanium

*Milena Stevanović [a], Marija Djošić [b], Ana Janković [a], Vesna Kojić [c],
Jovica Stojanović [b], Svetlana Grujić [a], Ivana Matić Bujagić [a],
Kyong Yop Rhee [d,**], Vesna Mišković-Stanković [a,*]*

[a] *Faculty of Technology and Metallurgy, University of Belgrade, Karnegijeva 4, 11000 Belgrade, Serbia*
[b] *Institute for Technology of Nuclear and Other Mineral Raw Materials, Bulevar Franš d'Eperea 86, Belgrade, Serbia*
[c] *Oncology Institute of Vojvodina, University of Novi Sad, Put Dr Goldmana 4, 21204 Sremska Kamenica, Serbia*
[d] *Department of Mechanical Engineering (BK21 Four), Kyung Hee University, Yongin 446-701, South Korea*

ARTICLE INFO

ABSTRACT

This paper describes a promising electrophoretic deposition (EPD) approach for developing composite coatings based on chitosan with the additional components of hydroxyapatite, graphene, and gentamicin on titanium substrate. Bioactive properties were investigated *in vitro* by immersing the coatings in simulated body fluid (SBF) at 37 °C. The newly formed biomimetic layer on the top of the deposited chitosan-based coatings on Ti was confirmed by X-ray diffraction, Fourier transform infrared spectroscopy, field emission scanning electron microscopy and electrochemical measurements, while coatings' bioactivity was proved by alkaline phosphatase activity assay in MRC-5 and L929 tested cell lines. The biocompatibility towards MRC-5 and L929 cell lines was investigated by dye exclusion test (DET) implying the non-cytotoxic effect of coatings. Gentamicin release studies were monitored during 21-day by high-performance liquid chromatography coupled with mass spectrometry, indicating rapid release of gentamicin ($\approx 40\%$) in the first 48 h and more than 60% after 14 days.

## 1. Introduction

Osseointegration can be defined as the formation of a direct structural and functional bond between the bone implant and the surrounding living tissue, inducing the growth of a new bone-like layer on the implant surface [1]. When designing bone implants, osseointegration ability is the primary requirement, besides functionality, that needs to be met. Moreover, bone implant materials are expected to be biocompatible and non-toxic, i.e., not to provoke strong immune reactions, for example, a "foreign-body" response [2]. The latest research papers have been devoted to devising new approaches for obtaining novel, as well as to the improvement

of existing bone implant materials [3—6]. For the development of medical implants aimed for applications such as bone fixation, dental reconstruction surgery, join replacement, stents, etc., titanium and titanium-based alloys are most often the materials of choice, thanks to their high strength, excellent corrosion resistance properties, ductility and toughness [7,8]. On the other side, titanium and its alloys, as inert metals, have biologically "passive" surface without bioactive or antibacterial properties [9,10].The high risk of bacterial infections during or after prosthetic interventions is another major threat, so it is very important to achieve the desired antibacterial activity of implanted material.

Various factors, such as infections, inflammation, stress shielding, can lead to implant failure. As it is reported in the literature [7], uncoated metal implants could even lead to rejection of implant due to bacterial colonization. There is a very large number of scientific papers dealing with the metal implants' surface modification, proving the efficiency in reduction of bacterial adhesion, inhibition of biofilm formation, and improving the bioactivity of the implants [11—13].

It is crucial for bone implant materials to be bioactive, that is to induce osteoblast adherence, growth, and proliferation on implant surface (osteoconductivity) and differentiation of immature cells i.e. osteoprogenitor cells into osteoblasts (osteoinductivity) and to possess appropriate mechanical properties. Based on the specified risks, the modification of the implant surface is necessary, in order to improve its biomedical application. Implant surface can be modified by different types of coatings using various techniques such as: thermal spray method [14], plasma spray technique [15], ion-beam deposition [16], pulsed-laser deposition [17,18], laser-induced hydrothermal synthesis [19], RF magnetron sputtering [20], micro-arc oxidation [21], using nanotubular surfaces [22—25], sol—gel [26,27], biomimetic process [28], and electrophoretic deposition [29—32].

Frequently-used electrophoretic deposition (EPD) technique represents a promising tool for coating the metal implant surface i.e. for combining antibacterial, bioactive properties of different materials with the mechanical stability of the metal substrate. This approach facilitates the much-needed biocompatible implant coating, avoiding the harmful ions release and scar tissue appearance. Moreover, EPD has stood out as a prospective "green" technique that allows the fabrication of composite coatings at room temperature, without the use of toxic chemicals [33].

The mineral phase in natural bones is hydroxyapatite (HAP), so called "bone apatite". Synthetic hydroxyapatite, being biocompatible and bioactive with high osteoinductive potential is the material of choice for implants' surface modification with the aim to improve the body acceptance of implants [34,35].

Considering the adhesive and antibacterial properties, the addition of natural polymers such as chitosan (CS) emerged as a promising tool for developing improved composite materials [36]. Innate antibacterial properties, biodegradability, superior adhesive properties, high biocompatibility, and promotion of cell differentiation and growth, classified CS as a valuable component of different composite biomaterials [37—39]. Furthermore, CS was shown to be an effective vehicle for the delivery of drugs and therapeutically active molecules that improves the antibacterial performance of composite materials [38,40]. Hydroxyapatite (HAP) is a widely used biomaterial, characterized by high biocompatibility and bioactivity but having poor mechanical, adhesive, and antibacterial properties, which can be easily supplemented by forming composites with different materials [35]. Combining the bioactive nature of HAP with desirable antibacterial and adhesive CS properties can allow the formation of composite biomaterials of improved biological performances [41—44]. Graphene addition to the ceramic/polymer matrix would improve on composites bioactivity and aid coatings structure to serve as drug carrier [45]. Recently, Fardi et al. [46] demonstrated that the addition of as little as 1 wt% graphene oxide to HAP coating contributed to the improved coating's crack and corrosion resistance, and immensely improved on adhesion strength of thus formed composite [46].

The "pressing" issue when load-bearing implants are used is the bacterial infections treatment and biofilm prevention. Gentamicin (Gent) is a proven highly-efficient antibiotic in the treatment of prosthetic infections caused by different bacteria and was thoroughly investigated as part of bone implant materials [29,30,47—49].

This study has focused on the in vitro investigation of the bioactivity of HAP/CS/Gr and HAP/CS/Gr/Gent coatings electrophoretically deposited on the Ti substrate, their cytotoxicity and gentamicin release study.

## 2. Experimental

### 2.1. Materials

Bare titanium foils (15 mm × 10 mm × 0.25 mm, 99.7%, Sigma—Aldrich, USA) were used as substrates for the electrophoretic deposition process. Starting suspensions for the EPD bath contained hydroxyapatite powder (particles <200 nm), chitosan (medium molecular weight 190—310 kDa, 75—85% deacetylation degree), pure graphene nanopowder (99.2%, nanoflakes), and gentamicin sulfate solution (50 mg/mL in dH$_2$O) — all purchased from Sigma—Aldrich, USA. Before EPD was performed, Ti foils were mechanically polished and ultrasonicated for 15 min in acetone followed by 5 min in ethanol. Ti foils were cut to dimensions 30 mm × 20 mm × 0.25 mm for electrochemical measurements, and 10 mm × 10 mm × 0.25 mm for gentamicin release studies. Gentamicin release measurements were performed using solvents that were HPLC grade (J.T. Baker, USA or Sigma—Aldrich, USA). GenPure ultrapure water system (TKA, Germany) was utilized for obtaining deionized from distilled water.

### 2.2. Electrophoretic deposition

HAP/CS/Gr aqueous suspension was prepared as follows: 1 wt % HAP powder was added in 0.05 wt% CS previously dissolved in 1% acetic acid solution, followed by addition of 0.01 wt% Gr under vigorous stirring; for HAP/CS/Gr/Gent aqueous suspension 0.1 wt% of gentamicin sulfate was added to the previously prepared HAP/CS/Gr suspension [29]. Both suspensions' pH values were measured to be 4.4. Electrochemical cell for deposition of HAP/CS/Gr and HAP/CS/Gr/

Gent coatings consisted of Ti foil serving as a working electrode (cathode) placed between two platinum panels (anodes) at an equal distance of 1.5 cm to ensure obtaining uniform coating on both sides of Ti plate. EPD was performed at a constant voltage of 5 V, and for deposition time of 12 min as a cataphoretic deposition process [29]. Further, deposited coatings were left to dry at room temperature for 24 h. The sample thicknesses were $3.0 \pm 1.5$ μm and $3.2 \pm 0.9$ μm for HAP/CS/Gr and HAP/CS/Gr/Gent coating, respectively.

### 2.3. FT-IR, XRD and FE-SEM

HAP/CS/Gr and HAP/CS/Gr/Gent coatings were immersed in the simulated body fluid (SBF) solution at 37 °C and pH = 7.4. The SBF solution was prepared by dissolving the reagent-grade salts: NaCl ($7.996$ g $L^{-1}$), NaHCO$_3$ ($0.350$ g $L^{-1}$), KCl ($0.224$ g $L^{-1}$), K$_2$HPO$_4$·3H$_2$O ($0.228$ g $L^{-1}$), MgCl$_2$·2H$_2$O ($0.305$ g $L^{-1}$), CaCl$_2$ ($0.278$ g $L^{-1}$) and Na$_2$SO$_4$ ($0.071$ g $L^{-1}$) in deionized water and buffered in tris(hydroxymethyl)aminomethane ($6.057$ g $L^{-1}$). pH was adjusted to 7.40 using 1 M hydrochloric acid (40 mL), at 37 °C [50].

After exposure to the SBF solution, coatings were taken out, dried at room temperature, and characterized using various techniques. Fourier transform infrared spectroscopy (FTIR), operating in ATR mode with a Nicolet IS-50 spectrophotometer (Thermo Fisher Scientific, USA, 400—4000 $cm^{-1}$ range, 4 $cm^{-1}$ spectral resolution) was employed to investigate the chemical bonding between components in composite coatings. Powder diffractometer Philips PW 1710 (Philips, Netherland) was utilized for X-ray diffraction analysis (XRD). The diffractometer was equipped with Ni-filtered Cu Kα radiation ($\lambda = 1.5418$ Å) and diffraction intensity was recorded at room temperature, between 4 and 70°, 0.05° step. Phase analysis was performed by PowderCell software. Field-emission scanning electron microscopy (FE-SEM) was performed in combined SE-BSE mode using LEO SUPRA 55 equipped with an In-Lens detector (Carl Zeiss AG, Germany) operating at 10 kV voltage acceleration.

### 2.4. Electrochemical measurements

Electrochemical characteristics of HAP/CS/Gr and HAP/CS/Gr/Gent coatings were investigated during a 28-day exposure to SBF by electrochemical impedance spectroscopy (EIS) and potentiodynamic sweep (PDS) electrochemical tests at 37 °C using a three-electrode, custom-made Plexiglas electrochemical cell, and the Reference 600™ potentiostat/galvanostat/ZRA (Gamry Instruments Inc., USA). The working electrode represented the coated Ti plate with a 1 cm$^2$ testing surface area, the counter electrode was a platinum mesh, whereas the reference was a saturated calomel electrode (SCE). The open circuit potential, $E_{ocp}$, measurements were run before each experiment until 0.01 mV $s^{-1}$ stability was achieved. The EIS data were obtained at the open circuit potential over the frequency range of 100 kHz—10 mHz, with the amplitude of 5 mV. Polarization curves were collected between $\pm 600$ mV *vs.* $E_{ocp}$, with a scan rate of 0.5 mV $s^{-1}$. Echem Analyst (Gamry Instruments Inc., USA) was utilized for curve fitting and data analysis. The measurements were repeated at least twice and then the representative measurement was chosen as an "average measurement". The curves and quantitative data of these measurements are then reported in the manuscript.

### 2.5. Cytotoxicity assay

The cytotoxicity assay was carried out by dye exclusion test (DET) towards human lung fibroblast MRC-5 (ATCC CCL-171) and mice fibroblast L929 (ATCC CRL-636) cell lines. Cells were cultured and propagated in the same manner as already published in our previous work [30]. Viable cells were seeded on the HAP/CS/Gr and HAP/CS/Gr/Gent coatings on Ti plates in 12-well plates (Costar) at concentration of $1 \times 10^5$/mL, whereas the control wells did not contain samples, only the seeded cells. Further, the coated samples with seeded cells were incubated at 37 °C under air flow with 5% CO$_2$, during the following 48 h. After the incubation, cells were separated from coated Ti plates by trypsinization method i.e. by adding 0.1% trypsin solution. The cell number and viability were further evaluated by the trypan blue exclusion method. Using a formula: $K = (N_s/N_k) \times 100\%$, where $N_k$ is the total number of cells (control) and $N_s$ is the number of cells on the tested Ti coated samples, growth inhibition was calculated and expressed as a percent of control.

### 2.6. Gentamicin release profiles

To estimate the total amount of gentamicin, the HAP/CS/Gr/Gent coatings were scraped off from the Ti substrate, and the obtained powders were completely dissolved in acidified deionized water. Gentamicin release studies were carried out during 21-day immersion in deionized water, at 37 °C, as a model system. All the measurements were done in triplicate. High-performance liquid chromatography (HPLC) (Thermo Fisher Scientific, USA) was utilized for gentamicin components separation and the detection and quantitative analysis was done in an ion trap mass spectrometer (MS) (LCQ Advantage, Thermo Fisher Scientific) with an electrospray ionizer. HPLC was equipped with a reverse-phase column (4.6 mm × 75 mm × 3.5 μm) Zorbax Eclipse® XDB-C18 (Agilent Technologies, USA), in front of which a precolumn (4.6 mm × 12.5 mm × 5 μm) was placed. Methanol (A), deionized water (B), and 10% acetic acid (C) comprised the mobile phase. The optimized HPLC and MS operating parameters (mobile-phase gradient, analytes' precursor ions, fragmentation reactions used for quantification, and optimal collision energies) for the determination of gentamicin compounds were published in our previous paper [49].

The gentamicin mass spectra were collected in the $m/z$ range of 50—1000. As expected, the MS spectrum revealed the three most abundant ions since gentamicin is composed of three compounds — gentamicin C1a, C2, and C1. These ions were further chosen as the precursor ions for each compound. Their most sensitive transitions were selected for quantification purposes. The presented gentamicin concentrations represent sums of the three determined gentamicin compounds.

### 2.7. Alkaline phosphatase activity

Abcam's Alkaline Phosphatase Assay Kit (Colorimetric) (ab83369) [51] is a simple and highly sensitive colorimetric assay aimed for the measurement of alkaline phosphatase

(ALP) activity in serum and biological samples. The detection kit was used to assess ALP levels in MRC-5 and L929 cells, as to evaluate the propensity of coated samples to stimulate biomineralization activity in tissues. The method is based on the dephosphorylation of the p-nitrophenyl phosphate (used as a phosphatase substrate) and its color change (yellow, $\lambda_{max}$ = 405 nm) by ALP. Alkaline phosphatase assay protocol included the addition of samples and standards to wells, followed by the addition of p-nitrophenyl phosphate solution only to the sample wells (not to standards) and ALP enzyme solution to standard wells (not to samples) and 60 min incubated. Absorbance of the tested solutions was measured at 405 nm using a microplate reader (Multiscan MCC340, Labsystems, Thermo Fisher Scientific, USA). All the measurements were done in triplicate to ensure the test reproducibility.

## 2.8. Statistical analysis

Statistical evaluation was performed for DET and ALP results using a one-way analysis of variance, followed by a multiple comparisons posthoc test. If the $p$-value was lower than 0.05, the results were considered statistically significant.

## 3. Results

### 3.1. In vitro bioactivity

Biomineralization is a naturally occurring process in living organisms that facilitates and controls the crystallization of minerals. It is based on the presence of organic matrices (such as collagen I in bone structure) and other soluble biomolecules that control and affect the crystal growth rate and morphology [52]. In the tissue engineering field this process serves as the basic criterion for the development and design of many new biomaterials that are intended to mimic the natural bone function. Nevertheless, when designing bone implant materials, one of the first steps in bioactivity evaluation is the assessment of biomaterials' ability to induce any effect on the living organism, examined through the in vitro experiments in SBF solution [50]. Although SBF environment contains only ions without any proteins or cells, some of the research papers [53,54] have demonstrated the high efficacy in the prediction of apatite ability formation when later compared with in vivo results. According to Zadpoor [55], 25/33 research studies results for in vitro and in vivo bioactivity testing in SBF were in good compliance. Taking into account the similarity of hydroxyapatite with the structure of the mineral part of natural bone, HAP-based coatings are expected to be bioactive and to possess the ability to induce the growth of a new apatite layer i.e. to promote osteoblast attachment, proliferation, and differentiation enhancing the biomaterial bioactivity and osseointegration [56,57]. In order to investigate the bioactivity of HAP/CS/Gr and HAP/CS/Gr/Gent coatings on titanium, we have performed FT-IR, XRD, FE-SEM and evaluated their properties via electrochemical measurements (EIS and PDS).

### 3.1.1. FT-IR

FT-IR spectra for the HAP/CS/Gr and HAP/CS/Gr/Gent coatings on titanium, before and after immersion in SBF at 37 °C for 7 days, are shown in Fig. 1a and b, respectively.

Differences in FT-IR bands position, for both HAP/CS/Gr and HAP/CS/Gr/Gent coatings before and after immersion indicated the new biomimetic HAP layer formation in SBF at 37 °C (Table 1). Bands in the 450–600 cm$^{-1}$ region represent the (O–P–O) bending modes in the phosphate group, while characteristic bands of the (P–O) stretching vibrations of the $PO_4^{3-}$ group can be observed in the 900–1200 cm$^{-1}$ region [29,30,49,58,59].

In HAP structure, hydroxyl and/or phosphate ions can be substituted by carbonate ions, leading to formation A-, B- or AB type of carbonate-substituted HAP [60]. Based on the position of carbonate bands in the FT-IR spectra for both HAP/CS/Gr and HAP/CS/Gr/Gent coatings after immersion in SBF at 37 °C for 7 days (Table 1), vibrational modes of O–C–O (878 cm$^{-1}$), and O–C groups (region 1400–1500 cm$^{-1}$) can be distinguished [29,30,60]. The position of these carbonate bands, confirmed that the AB-type substitution in newly-formed HAP occurred [29,61]. Carbonate-substituted hydroxyapatite is well-known for its bioactivity [62]. Bands assigned to the structural OH$^-$ bending also confirmed HAP structure [58].

The presence of carbonate-substituted HAP on the top of the investigated coatings is preferred for numerous reasons. The fact that carbonate-substituted HAP is already found in the natural bone and dentine tissue can stand out as the most important reason [63].

### 3.1.2. XRD

XRD analysis also confirmed the formation of carbonate-substituted HAP after 7-day immersion in SBF, supporting the FT-IR results. Fig. 1c and d represents the XRD patterns for HAP/CS/Gr and HAP/CS/Gr/Gent coatings before and after soaking in SBF at 37 °C for 7 days, respectively. Diffraction maxima were identified by standard JCPDS file no. 09-0432 for HAP and standard JCPDS file no. 89-2762 for titanium (coatings' substrate). As it was reported in our previously published papers, the crystallite domain size for both as-deposited HAP/CS/Gr [29] and HAP/CS/Gr/Gent [29,31] coatings was calculated to be 43.5 and 31.1 nm, respectively. According to the diffraction maxima broadening, it could be concluded that newly formed HAP on the top of both HAP/CS/Gr and HAP/CS/Gr/Gent coatings after soaking in SBF consisted of very fine crystallites. To confirm this statement, the crystallite domain size for both newly grown HAP on the top of HAP/CS/Gr and HAP/CS/Gr/Gent coatings was calculated to be 16.6 and 36.0 nm, respectively [31].

Carbonate ions can substitute OH$^-$ (A-type), $PO_4^{3-}$ (B-type), or both OH$^-$ and $PO_4^{3-}$ (AB-type substitution, found in biological apatites) [29,30,64–66] ions in HAP lattice, causing the changes in unit cell parameters and crystallinity [67]. A-type substitution is known to cause $a$-axes expansion and $c$-axes contraction as opposed to B-type substitution that causes a
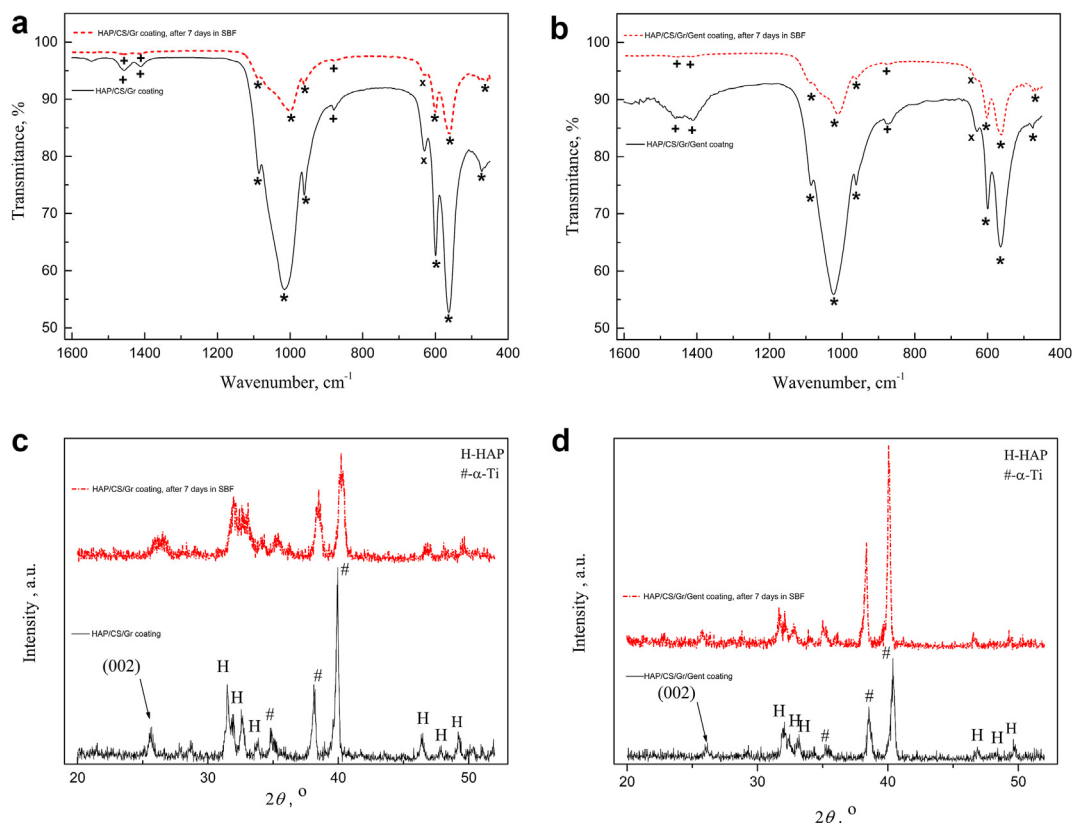
Fig. 1 − FT-IR spectra of (a) HAP/CS/Gr and (b) HAP/CS/Gr/Gent coatings (bands denotation: * $PO_4^{3-}$; + $CO_3^{2-}$; x $OH^-$) in the region from 450 to 1600 cm$^{-1}$ and XRD patterns for (c) HAP/CS/Gr and (d) HAP/CS/Gr/Gent coatings, in the region from 20 to 50 $2\theta$, before and after soaking in SBF at 37 °C for 7 days.

contraction in $a$-axes and expansion in $c$-axes [64]. It was calculated that newly formed HAP on HAP/CS/Gr coating, obtained after immersion in SBF, exhibited the changes in both $a$ (9.390 Å) and $c$ (6.871 Å) axes in respect to the values of $a$ (9.446 Å) and $c$ (6.907 Å) for HAP/CS/Gr coating before immersion in SBF [29]. In the case of newly formed HAP on the HAP/

CS/Gr/Gent coating the changes in both unit cell parameters $a$ (9.451 Å) and $c$ (6.912 Å) were observed in respect to the HAP/CS/Gr/Gent coating before immersion ($a$-9.383 Å, $c$-6.863 Å [29]), suggesting the presence of AB-type carbonate substitution in the newly formed HAP. According to the literature [68], values of HAP unit cell parameters are as follows: $a = 9.418$ Å,

Table 1 − Characteristic bands positions and vibration assignments of coatings' FTIR spectra before and after immersion in SBF at 37 °C for 7 days.

| Assignments | Coating | | | |
|---|---|---|---|---|
| | Before SBF | | After SBF | |
| | HAP/CS/Gr | HAP/CS/Gr/Gent | Biomimetic HAP on HAP/CS/Gr | Biomimetic HAP on HAP/CS/Gr/Gent |
| | Wavenumber, cm$^{-1}$ [29] | | Wavenumber, cm$^{-1}$ [29,30,49,58−62] | |
| Vibrational modes of $PO_4^{3-}$ group | 473 | 474 | 475 | 474 |
| | 563 | 562 | 561 | 562 |
| | 600 | 600 | 600 | 601 |
| | 952 | 962 | 960 | 961 |
| | 1020 | 1024 | 1001 | 1012 |
| | 1085 | 1085 | 1087 | 1088 |
| Vibrational modes of $CO_3^{2-}$ group | 878 | 878 | 878 | 878 |
| | 1411 | 1411 | 1414 | 1412 |
| | 1459 | 1458 | 1456 | 1457 |
| Vibrational mode of structural $OH^-$ group | 632 | 634 | 628 | 631 |

$c = 6.884$ Å (JCPDS 09-0432). The difference between theoretical and experimental values in $a$- and $c$-axis is greater in the case of newly formed HAP on the top of the HAP/CS/Gr/Gent coating, suggesting that more hydroxyl and phosphate ions were substituted by carbonate ions, compared to newly grown HAP on the antibiotic-free coating (HAP/CS/Gr).

The Ca/P ratios according to the energy dispersive spectrometry (EDS) analysis (data not shown) were calculated to be 1.61 and 1.36, for HAP/CS/Gr and HAP/CS/Gr/Gent coatings, before immersion in SBF, respectively. After immersion in SBF, Ca/P ratio has lower value for both coatings, e.g. 1.52 and 1.24 for HAP/CS/Gr and HAP/CS/Gr/Gent, respectively, confirming the formation of new biomimetic HAP layer on the top of both coatings. Since the value of Ca/P ratio in stoichiometric HAP is 1.67 [69], the lower obtained values of Ca/P ratio proved that newly formed HAP on both coatings is carbonate-substituted [70,71]. Due to the lower Ca/P ratio in the case of HAP grown on the top of the HAP/CS/Gr/Gent coating (1.24) with respect to the HAP on the top of the coating without antibiotic (1.52), the additional confirmation of the greater carbonate substitution in the HAP crystallite formed on the top of the coating with antibiotic was achieved.

These results are quite promising as it is known that carbonate substituted HAP can improve the biological performances of prosthetic implant materials (bioactivity, osteoconductivity, growth, and differentiation of osteoblast cells) with respect to the stoichiometric HAP [72,73] due to the presence of carbonate ions in HAP structure which contribute to the increased HAP solubility and simultaneously reduced HAP crystallinity [74].

### 3.1.3.   FE-SEM
It is known that after immersion in SBF, the concentration of calcium and phosphate ions on the coatings' surface increases, providing conditions for the growth of a new biomimetic HAP layer through the simultaneous dissolution and precipitation reactions [75]. The dissolution and precipitation of HAP in SBF are reversible reactions [76—78]. The micrographs of HAP/CS/Gr and HAP/CS/Gr/Gent coatings after immersion in SBF for 7 days, are represented in Fig. 2 with their corresponding images before SBF given as insets (Fig. 2a and b, respectively). The presence of newly formed HAP in the form of characteristic spherical agglomerates on the top of both

HAP/CS/Gr and HAP/CS/Gr/Gent coating can be clearly distinguished from Fig. 2.

### 3.2.   Electrochemical characteristics

Electrochemical measurements, i.e. electrochemical impedance spectroscopy (EIS) and potentiodynamic sweep (PDS) tests were performed on HAP/CS/Gr and HAP/CS/Gr/Gent coatings as they can provide valuable information about the new HAP layer appearance after immersion in SBF. Monitoring the electrochemical parameters over a prolonged period (28 days) in physiological media should predict the possible behavior of composite coatings in the human body.

### 3.2.1.   EIS
Electrochemical impedance was monitored during the 28-day exposure to SBF and the resulting Bode modulus graphs for certain representative periods are shown in Fig. 3. Both HAP/CS/Gr and HAP/CS/Gr/Gent coatings exhibited increased impedance values for the duration of the experiment due to the growth of a new biomimetic HAP layer as explained in Sections 3.1.1.—3.1.3. (FT-IR, XRD, FE-SEM). The highest impedance increase that suggested the most intensive growth of HAP layer was achieved after 4 days. Since biomineralization is a complex process consisting of simultaneous coating dissolution and calcium phosphates precipitation [76], the dominant reaction in this initial period can be ascribed to the agglomerates precipitation of the newly formed HAP. This phenomenon can be explained by the high initial concentration gradient between the SBF medium and the immersed coating as well as the solubility of the particles in SBF, leading to the HAP precipitation. Later on, the increase in impedance was much slower indicating the slower growth of the new HAP layer.

To gain a better insight into the electrochemical parameters for the investigated samples, obtained experimental impedance data were fitted using the equivalent electrical circuit (EEC) presented in Fig. 4. This type of EEC is generally used to explain the properties of coated metal samples, including the bioactive HAP-based coatings on titanium [49]. The elements of the chosen EEC in Fig. 4 are schematically depicted along with the components of the physical system they represent, i.e., ohmic resistance of the SBF electrolyte, $R_\Omega$,
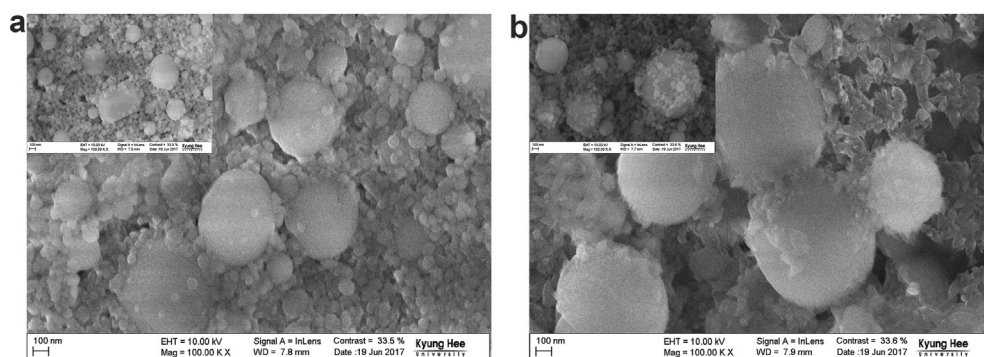


**Fig. 2 — FE-SEM micrographs of (a) HAP/CS/Gr and (b) HAP/CS/Gr/Gent coatings after 7-day soaking in SBF at 37 °C (Insets: corresponding coatings before immersion in SBF).**
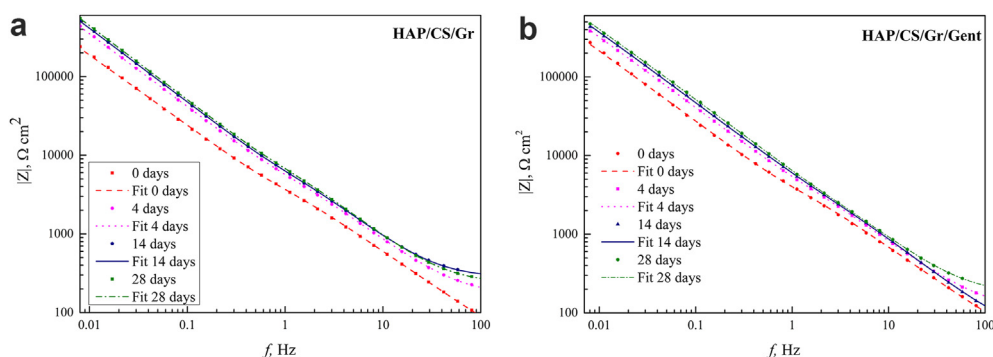
Fig. 3 — Bode modulus plots for (a) HAP/CS/Gr and (b) HAP/CS/Gr/Gent coatings during 28-day exposure to SBF at 37 °C.

followed by the parallel circuit consisting of the constant phase element related to the coating capacitance, $CPE_c$, and the coating pore resistance, $R_p$. The final element represents the electrical properties of the metal itself, i.e. the double layer formed on the metal/electrolyte interface, depicted by charge-transfer resistance, $R_{ct}$, and constant phase element related to the double-layer capacitance, $CPE_{dl}$.

The impedance of a CPE element ($Z_{CPE}$) can be expressed using Eq. (1) [79], where $Y_0^{-1}$ is the admittance, $\omega$ is the angular frequency, $\alpha$ is a parameter which quantifies the deviation from an ideal capacitor and $i^2 = -1$. The capacitance value can be calculated using Eq. (2), where $\omega_{max}$ is the angular frequency at which the imaginary component of the impedance reaches its maximum [79]. It is obvious that for $\alpha$ values close to unity, $C_{CPE} = Y_0$. As in our case $\alpha$ was always higher than 0.8, $Y_0$ values obtained from the fit were used as the coating and double layer capacitances without further calculations. The impedance data in the complex plane was well fitted by the proposed EEC. A suitably low goodness of fit ($\chi^2$) in the $10^{-6}$–$10^{-4}$ range and relatively low percentage error related to each element (less than 10%) were obtained. The acquired results confirmed the applicability of the proposed model to the investigated systems.

$$Z_{CPE} = Y_0^{-1} \cdot (i \cdot \omega)^{-\alpha} \qquad (1)$$

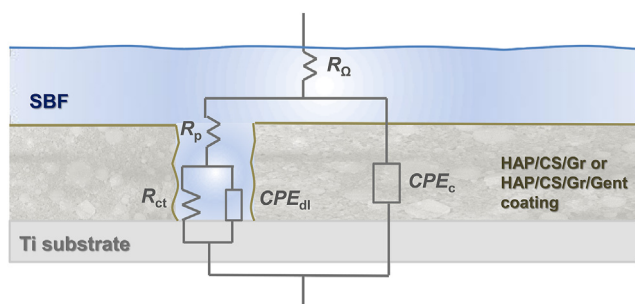$$C_{CPE} = Y_0 (\omega_{max})^{\alpha - 1} \qquad (2)$$



Fig. 4 — Schematic representation of the HAP/CS/Gr and HAP/CS/Gr/Gent-coated titanium in SBF, along with the scheme of the equivalent electrical circuit used for impedance plots fitting.

The formation and growth of the new apatite layer on the HAP/CS/Gr and HAP/CS/Gr/Gent coatings surfaces during the 28-day exposure to SBF is directly related to the quantitative values for coating pore resistance, $R_p$, and coating capacitance, $C_c$, which were obtained by EIS fitting and presented in Fig. 5.

From Fig. 5, the rapid increase in $R_p$ values and rapid decrease in $C_c$ (for both coatings) were observed during the first couple of days, indicating the coating thickness increase due to the precipitation and growth of the newly formed HAP layer. After the first 4 days, the $R_p$ increase and $C_c$ decrease became slower, which is in accordance with previously discussed impedance values (Fig. 3).

### 3.2.2. PDS

The bioactive nature of HAP/CS/Gr and HAP/CS/Gr/Gent coatings, when exposed to SBF solution for 28 days, was also assessed using polarization measurements that gave insight into valuable corrosion parameters. Fig. 6 represents the polarization curves for HAP/CS/Gr and HAP/CS/Gr/Gent coatings at the very beginning (0 days) and the end (28 days) of exposure to the SBF solution.

The cathodic curves were linear over one decade of current (Fig. 6), so they were extrapolated in order to determine the values of the corrosion current density, $j_{corr}$, and the cathodic Tafel slopes, $b_c$, were calculated from their slopes. On the other hand, the anodic parts of the polarization curves did not exhibit sufficiently linear behavior due to the changing nature of the anodic reactions, and they could not be used either for $j_{corr}$ calculation, nor to obtain the anodic Tafel slope. The corrosion current density significantly decreased for both samples after 28-day exposure — ten fold decrease for HAP/CS/Gr (from 0.17 to 0.016 $\mu A\,cm^{-2}$) and HAP/CS/Gr/Gent (from 0.14 to 0.043 $\mu A\,cm^{-2}$) which can be explained by improved corrosion stability of the newly formed biomimetic HAP layer, as already indicated by FT-IR, XRD and FE-SEM (Sections 3.1.1.–3.1.3.). The cathodic Tafel slopes, $b_c$, did not change significantly from 0 to 28 days for both coatings; in the case of HAP/CS/Gr from −220 to −215 mV dec$^{-1}$, and for HAP/CS/Gr/Gent from −276 to −264 mV dec$^{-1}$, meaning that the reaction mechanism did not change during prolonged exposure to SBF. Carefully considering all the electrochemical results obtained from EIS and PDS, i.e. increase in $R_p$ and decrease in $C_c$ and $j_{corr}$, it can be concluded that both HAP/CS/Gr and HAP/CS/Gr/
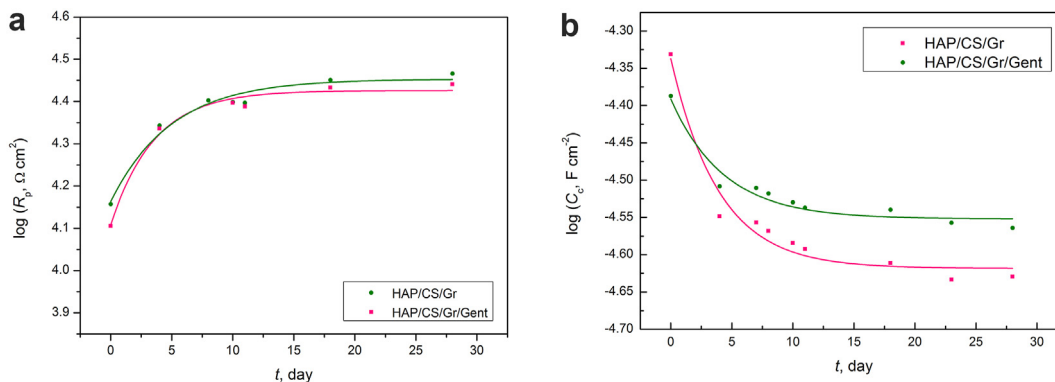
**Fig. 5 — Time dependence of (a) coating pore resistance, $R_P$ and (b) coating capacitance, $C_c$, for HAP/CS/Gr and HAP/CS/Gr/Gent coatings during a 28-day exposure to SBF at 37 °C.**

Gent coatings showed a tendency to promote the growth of new HAP layer growth after exposure to physiological solute-ions.

### 3.3. Biocompatibility

Fig. 7 represents the results of the trypan blue DET test that was performed on two fibroblast cell lines — human MRC-5 and mouse L929 to estimate the proportion of viable cells in the presence of HAP/CS/Gr and HAP/CS/Gr/Gent coatings.

Trypan blue DET test is an efficient and simple method that is based on cell staining after their mixing with the solution of a dye. The evaluation of cell growth (% K) was expressed as a percent of control and further estimated based on the ratio of stained and unstained cells since damaged cells were stained as opposed to undamaged which were unstained. HAP/CS/Gr coating provoked the inhibition of growth neither in the case of MRC-5 (92.2%) nor for L929 (96.4%). After the gentamicin introduction, the cell growth appeared to decrease slightly for both MRC-5 (83.1%) and L929 (79.7%) cell lines but still within acceptable cytotoxicity limits. Slight drop in survival rate was

attributed to the antibiotic presence, as well documented in a recent study when high concentrations of therapeutic agent — gentamicin (250—270 μg/mL) which was reached during the immersion of the gentamicin containing films affected oste-oblastic proliferation (MC3T3-E1 cells) when compared to the control [80].

One-way analysis of variance statistical tests, when applied to the DET test, pointed out that the differences in the cell growth for both MRC-5 and L929 cell lines between the two samples were statistically significant ($p < 0.05$).

### 3.4. Gentamicin release studies

Loading the antibacterial agents into composite structures minimizes the applied doses, reduces the cytotoxicity, and facilitates the sustained release and drug availability. HPLC-MS was utilized for the assessment of total (overall) genta-micin amount transferred into composite coatings by EPD, and for investigation of gentamicin release under appropriate conditions that mimic the physiological conditions. The total amount of gentamicin in the HAP/CS/Gr/Gent coating per 1 cm$^2$ was determined by HPLC-MS preceded by scraping off the coating and dissolving it in slightly acidified dH$_2$O. The measured amount was 13.9 μg. Further, the release of genta-micin from the HAP/CS/Gr/Gent coating in deionized water was studied during the 21-day immersion. The average cu-mulative release profile is shown in Fig. 8a. The highly desired effect of the initial burst-release of gentamicin was man-ifested during the first 7 days, when ~60% was released in such a short period and may be promising for the initial protection of implants from bacterial cell adhesion and biofilm forma-tion. The rapid release of gentamicin was followed by a slower release rate reaching up to 74% after 21 days. The gentamicin release profile could clearly be divided into two different stages. The antibiotic release in the first stage (first 7 days), where the initial burst effect of gentamicin release was noticed, was probably a consequence of the surface adsorbed gentamicin molecules diffusion. The second stage (7—21 days) was characterized by a controlled and sustained release of gentamicin which could be associated with the gentamicin diffusion through the coating pores, i.e. the penetration of the release medium into the coating pores, dissolving the drug, and ensuring a slower release rate.
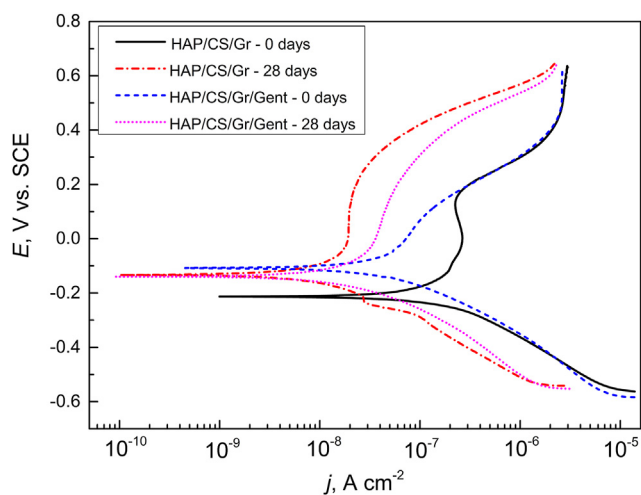


**Fig. 6 — Potentiodynamic polarization curves of HAP/CS/Gr and HAP/CS/Gr/Gent coatings before and after 28-day immersion in SBF at 37 °C.**
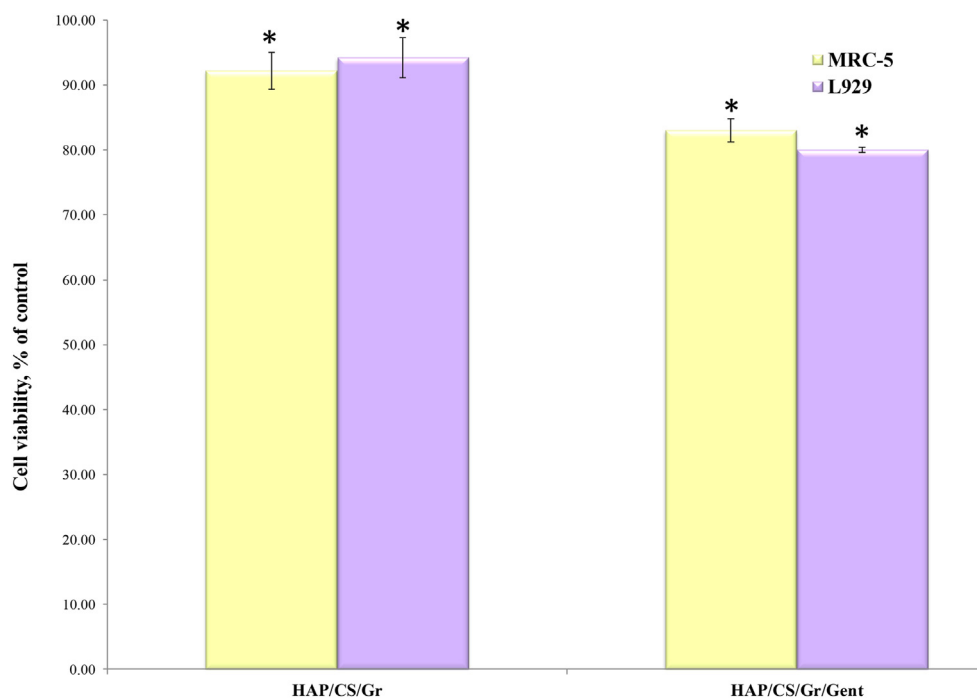
Fig. 7 — **Inhibition of MRC-5 and L929 cell growth (expressed as a percent of control) when exposed to HAP/CS/Gr and HAP/CS/Gr/Gent coatings.**

Experimental data were fitted and compared with the Korsmeyer—Peppas and early time approximation (ETA) kinetic models of release. Korsmeyer—Peppas model [81] (Eq. (3)) is described by the ratio of the current mass of gentamicin ($m_t$) released at time $t$, and the total initial mass of gentamicin, $m_{tot}$, whereas $k_{KP}$ is the Korsmeyer—Peppas constant, particular to the investigated coating material, and $n$ is the coefficient that indicates the diffusion mechanism ($n \sim 0.5$ — Fickian and $n > 0.5$ — non-Fickian). The Korsmeyer—Peppas model was applied in its linear form, where the data were transformed to the logarithmic scale (Eq. (4)).

$$\frac{m_t}{m_{tot}} = k_{KP} \cdot t^n \tag{3}$$

$$\log \frac{m_t}{m_{tot}} = \log k_{KP} + n \cdot \log t \tag{4}$$

The obtained Korsmeyer—Peppas graph (Fig. 8b) was used to calculate the value of exponent $n$ from the slope of the curve and it was 0.392. This result pointed out that the gentamicin release process followed the Fick's diffusion law and that it was therefore affected by the concentration gradient of gentamicin in the composite matrix.

After the governing mechanism of gentamicin release was estimated, we employed another kinetic model — early time approximation (ETA) which describes the active substance release following Fickian diffusion law from thin polymer/composite samples. According to Ritger and Peppas [82] this model is suitable for one-dimensional release from thin films. This approximation model is valid for the first 60% of release [82] and represents a useful method for the calculation of the diffusion coefficient of the gentamicin release process. Since ~60% of gentamicin release was achieved within the first 14

days (64%) the ETA approximation was applied for this period. ETA is described by Eq. (5) with the following parameters: $m_t$ — the mass of gentamicin released from the coating at the time, $m_{tot}$ — the total initial gentamicin mass inside the coating, $D$ — gentamicin diffusion coefficient, $t$ — time, and $\delta$ — coating thickness.

$$\frac{m_t}{m_{tot}} = 4 \cdot \left( \frac{Dt}{\pi \delta^2} \right)^{1/2} \tag{5}$$

Fig. 8c shows the ETA model applied to the experimental release data (in the first 14 days) for HAP/CS/Gr/Gent coating. The diffusion coefficient, $D$, was calculated to be $4.5 \times 10^{-14}$ cm$^2$ s$^{-1}$, indicating a slow gentamicin release from the coating within the first 14 days. Comparing the obtained diffusion coefficient for gentamicin release from HAP/CS/Gr/Gent coating with the previously published coefficient for HAP/CS/Gent coating ($D = 2.4 \times 10^{-14}$ cm$^2$ s$^{-1}$) [49] it was noticeable that HAP/CS/Gr/Gent coating exhibited almost twice as fast release contrary to HAP/CS/Gent coating. This conclusion supports the results for the total gentamicin concentration in HAP/CS/Gr/Gent coating that exhibited a higher value (13.9 μg) compared to HAP/CS/Gent coating [49] (9.4 μg), implying that Gr addition improves the gentamicin loading, while also causing faster release from the coating. The use of graphene as a drug carrier is the subject of a lot of research owing to its high surface area enabling the drug loading on both sides of the Gr sheet [83—85]. This could be an explanation of a higher rate of gentamicin loading in HAP/CS/Gr/Gent coating compared to HAP/CS/Gent coating.

Gentamicin mechanism of action relies on aminoglycoside antibiotic irreversibly binding to a specific subunit proteins (30S) and 16S rRNA in the bacterial cell that causes t-RNA
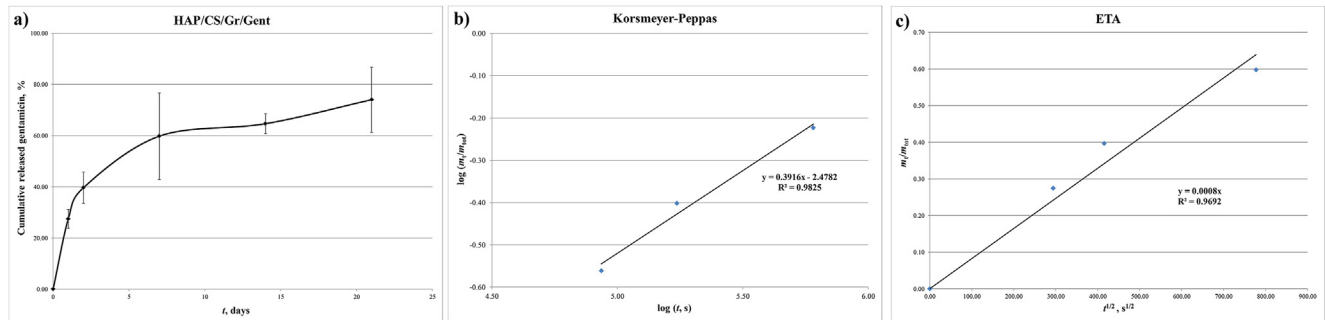
**Fig. 8 − (a) The average cumulative release profile of gentamicin, (b) Korsmeyer−Peppas model and (c) early time approximation (ETA) applied to the gentamicin-release profile from HAP/CS/Gr/Gent coating.**

misreading that prevents the synthesis of vital proteins. More precisely, gentamicin binds to four 16S rRNA nucleotides and a protein S12 amino acid, causing interference in the decoding site. Finally, the misreading of mRNA causes incorrect amino acids to be inserted into the polypeptide chain [86]. When analyzing the results of gentamicin release profiles (Fig. 8a) side by side with our previously published results related to the antibacterial activity of HAP/CS/Gr/Gent coating, which was verified as highly efficient against *Staphylococcus aureus* TL and *Escherichia coli* ATCC 25922 judging by wide inhibition zones in agar-diffusion test as a direct evidence of Gent leaching into the surrounding medium [29], an interesting correlation could be observed. HAP/CS/Gr/Gent coating exhibited a strong antibacterial effect against two tested bacterial strains, particularly well pronounced against *S. aureus*, causing the complete reduction of bacterial cells after only 3 h of exposure (from $5.66 \times 10^2$ to 0 CFU mL$^{-1}$), while in the case of *E.coli* significant reduction (from $1.46 \times 10^6$ to $2.53 \times 10^3$ CFU mL$^{-1}$) during the 24-h exposure was noticed.

The rapid and strong antibacterial effect monitored during the first 24 h coincides with the initial burst effect of gentamicin observed on the cumulative release profile (Fig. 8a).

### 3.5. Alkaline phosphatase assay

Alkaline phosphatase activity represents a valuable biochemical marker and an important sign of osteogenic differentiation. ALP is a ubiquitous enzyme that is present in different tissues of the human body, especially in liver and bone cells. The ALP level affects the bone mineralization process, but the precise mechanism is still questionable. Possible mechanisms involve the hydrolysis of phosphate esters by ALP and an increase of local concentration of phosphate ions at mineralization sites, promoting the calcification. Another mechanism proposes that ALP affects the calcification process by destroying inorganic pyrophosphate that inhibits mineral formation [87,88]. When designing the bone implant materials it is of particular relevance that the
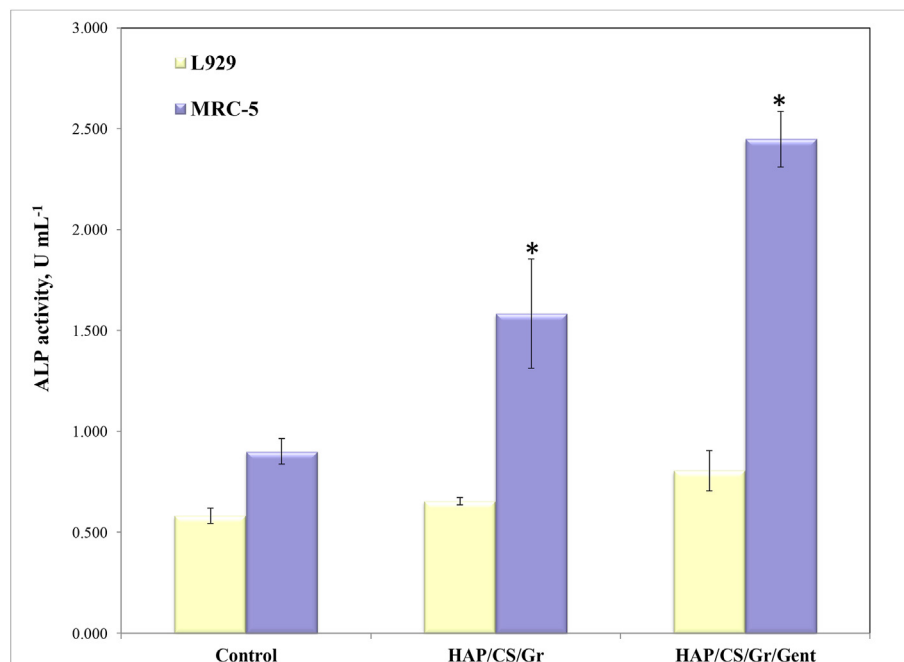


**Fig. 9 − ALP levels in MRC-5 in L929 cell extracts in the presence of HAP/CS/Gr and HAP/CS/Gr/Gent coatings. *$p < 0.05$ for the respective cell line.**

proposed material possesses bioactive properties, i.e. the ability to induce osseointegration. An important step in evaluating the osseopromotive properties of deposited HAP/CS/Gr and HAP/CS/Gr/Gent coatings is the estimation of the ALP expression potential in osteoblast cells. Since the cytotoxicity studies were performed on non-specific fibroblast cell lines — MRC-5 and L929, ALP studies were also conducted on these, allowing an initial assessment of mineralization. Fig. 9 represents the results of ALP assay for HAP/CS/Gr and HAP/CS/Gr/Gent coatings.

When comparing the results of ALP level for HAP/CS/Gr and HAP/CS/Gr/Gent coatings for investigated cell extracts (MRC-5 and L929) with control, the statistically significant ($p < 0.05$) increase for both samples was noticed. MRC-5 fibroblast cell line exhibited higher ALP values contrary to the L929 cell line in the presence of both samples. The coating loaded with antibiotic, HAP/CS/Gr/Gent, expressed higher ALP potential (2.449 U/mL for MRC-5 and 0.805 U/mL for L929) as opposed to its counterpart HAP/CS/Gr coating (1.584 U/mL for MRC-5 and 0.654 U/mL for L929). Based on the presented ALP data both samples possess high biomineralization potential even in the case of non-specific fibroblast cell lines. High ALP levels in cell extracts represent encouraging prospects of the HAP/CS/Gr and HAP/CS/Gr/Gent coatings for further investigation towards tissue-specific cell lines.

## 4.　　Conclusions

Titanium surface was modified by applying new composite, biocompatible, and bioactive hydroxyapatite/chitosan coatings with and without gentamicin using the electrophoretic deposition technique (HAP/CS/Gr and HAP/CS/Gr/Gent, respectively). Bioactive properties of deposited coatings were confirmed by the biomimetic growth of a new HAP layer of AB-type substituted on the both coating surfaces after 7-day exposure to SBF solution at 37 °C, using the XRD, FT-IR, FE-SEM, electrochemical impedance spectroscopy and potentiodynamic sweep measurements. DET test, as well as ALP test, towards MRC-5 and L929 cell lines also proved high bioactive potential of both coatings. The gentamicin-containing coating exhibited the highest ALP levels when compared with its counterpart without gentamicin and the control. *In vitro* gentamicin release in SBF solution at 37 °C indicated initial burst-release effect during the first 7 days, when ~60% was released followed by a slower release process reaching up to 74% after 21 days. According to the early-time approximation (ETA) model, the gentamicin diffusion coefficient, D, during the first period was calculated to be $4.5 \times 10^{-14}$ cm$^2$ s$^{-1}$.

Based on all represented results it could be proposed that both chitosan-based coatings electrodeposited on Ti are promising biomaterials for further investigation and potential biomedical application as hard tissue implants.

## Declaration of Competing Interest

The authors declare that they have no known competing financial interests or personal relationships that could have appeared to influence the work reported in this paper.

REFERENCES

[1] Mello AS da S, dos Santos PL, Marquesi A, Queiroz TP, Margonar R, de Souza Faloni AP. Some aspects of bone remodeling around dental implants. Rev Clín Periodoncia Implantol y Rehabil Oral 2018;11:49–53. https://doi.org/10.1016/j.piro.2015.12.001.

[2] Mariani E, Lisignoli G, Borzì RM, Pulsatelli L. Biomaterials: foreign bodies or tuners for the immune response? Int J Mol Sci 2019;20. https://doi.org/10.3390/ijms20030636.

[3] Harun WSW, Asri RIM, Alias J, Zulkifli FH, Kadirgama K, Ghani SAC, et al. A comprehensive review of hydroxyapatite-based coatings adhesion on metallic biomaterials. Ceram Int 2018;44:1250–68. https://doi.org/10.1016/j.ceramint.2017.10.162.

[4] Furkó M, Balázsi K, Balázsi C. Comparative study on preparation and characterization of bioactive coatings for biomedical applications - a review on recent patents and literature. Rev Adv Mater Sci 2017;48:25–51.

[5] Luo Y, Jiang Y, Zhu J, Tu J, Jiao S. Surface treatment functionalization of sodium hydroxide onto 3D printed porous Ti6Al4V for improved biological activities and osteogenic potencies. J Mater Res Technol 2020;9:13661–70. https://doi.org/10.1016/j.jmrt.2020.09.076.

[6] Wang J, Pan Y, Feng R, Cui H, Gong B, Zhang L, et al. Effect of electrolyte composition on the microstructure and bio-corrosion behavior of micro-arc oxidized coatings on biomedical Ti6Al4V alloy. J Mater Res Technol 2020;9:1477–90. https://doi.org/10.1016/j.jmrt.2019.11.073.

[7] Priyadarshini B, Rama M, Chetan, Vijayalakshmi U. Bioactive coating as a surface modification technique for biocompatible metallic implants: a review. J Asian Ceram Soc 2019;7:397–406. https://doi.org/10.1080/21870764.2019.1669861.

[8] Nicholson JW. Titanium alloys for dental implants: a review. Prosthesis 2020;2:100–16. https://doi.org/10.3390/prosthesis2020011.

[9] Souza JCM, Sordi MB, Kanazawa M, Ravindran S, Henriques B, Silva FS, et al. Nano-scale modification of titanium implant surfaces to enhance osseointegration. Acta Biomater 2019;94:112–31. https://doi.org/10.1016/j.actbio.2019.05.045.

[10] Xiao M, Chen YM, Biao MN, Zhang XD, Yang BC. Bio-functionalization of biomedical metals. Mater Sci Eng C 2017;70:1057–70. https://doi.org/10.1016/j.msec.2016.06.067.

[11] Ahn TK, Lee DH, Kim T-Sup, Jang G Chol, Choi SJ, Oh JB, et al. Modification of titanium implant and titanium dioxide for bone tissue engineering. Adv Exp Med Biol 2018;1077:355–68. https://doi.org/10.1007/978-981-13-0947-2_19.

[12] Asri RIM, Harun WSW, Samykano M, Lah NAC, Ghani SAC, Tarlochan F, et al. Corrosion and surface modification on biocompatible metals: a review. Mater Sci Eng C 2017;77:1261–74. https://doi.org/10.1016/j.msec.2017.04.102.

[13] Zhang LC, Chen LY, Wang L. Surface modification of titanium and titanium alloys: technologies, developments, and future interests. Adv Eng Mater 2020;22:1—37. https://doi.org/10.1002/adem.201901258.

[14] Kaur S, Bala N, Khosla C. Characterization of thermal-sprayed HAP and HAP/TiO2 coatings for biomedical applications. J Therm Spray Technol 2018;27:1356—70. https://doi.org/10.1007/s11666-018-0766-3.

[15] Heimann RB. Plasma-sprayed hydroxylapatite coatings as biocompatible intermediaries between inorganic implant surfaces and living tissue. J Therm Spray Technol 2018;27:1212—37. https://doi.org/10.1007/s11666-018-0737-8.

[16] Zykova A, Safonov V, Dudin S, Yakovin S, Donkov N, Ghaemi MH, et al. Structural and mechanical properties of hydroxyapatite coatings formed by ion-beam assisted deposition. J Phys Conf Ser 2018;992:012035. https://doi.org/10.1088/1742-6596/992/1/012035.

[17] Duta L, Popescu AC. Current status on pulsed laser deposition of coatings from animal-origin calcium phosphate sources. Coatings 2019;9:335. https://doi.org/10.3390/coatings9050335.

[18] Ahmed MK, Ramadan R, Afifi M, Menazea AA. Au-doped carbonated hydroxyapatite sputtered on alumina scaffolds via pulsed laser deposition for biomedical applications. J Mater Res Technol 2020;9:8854—66. https://doi.org/10.1016/j.jmrt.2020.06.006.

[19] Um SH, Chung YW, Seo Y, Seo H, Ok MR, Kim YC, et al. Robust hydroxyapatite coating by laser-induced hydrothermal synthesis. Adv Funct Mater 2020;30:1—11. https://doi.org/10.1002/adfm.202005233.

[20] Safavi MS, Surmeneva MA, Surmenev RA, Khalil-Allafi J. RF-magnetron sputter deposited hydroxyapatite-based composite & multilayer coatings: a systematic review from mechanical, corrosion, and biological points of view. Ceram Int 2021;47:3031—53. https://doi.org/10.1016/j.ceramint.2020.09.274.

[21] Wang X, Mei L, Jiang X, Jin M, Xu Y, Li J, et al. Hydroxyapatite-coated titanium by micro-arc oxidation and steam—hydrothermal treatment promotes osseointegration. Front Bioeng Biotechnol 2021;9:1—12. https://doi.org/10.3389/fbioe.2021.625877.

[22] Radtke A. Photocatalytic activity of titania nanotube coatings enriched with nanohydroxyapatite. Biomed J Sci Tech Res 2019;15:11408—12. https://doi.org/10.26717/bjstr.2019.15.002711.

[23] Qadir M, Li Y, Biesiekierski A, Wen C. Surface characterization and biocompatibility of hydroxyapatite coating on anodized TiO2 nanotubes via PVD magnetron sputtering. Langmuir 2021;37:4984—96. https://doi.org/10.1021/acs.langmuir.1c00411.

[24] Gunputh UF, Le H, Besinis A, Tredwin C, Handy RD. Multilayered composite coatings of titanium dioxide nanotubes decorated with zinc oxide and hydroxyapatite nanoparticles: controlled release of Zn and antimicrobial properties against staphylococcus aureus. Int J Nanomedicine 2019;14:3583—600. https://doi.org/10.2147/IJN.S199219.

[25] Chernozem RV, Surmeneva MA, Krause B, Ignatov VP, Prymak O, Loza K, et al. Functionalization of titania nanotubes with electrophoretically deposited silver and calcium phosphate nanoparticles: structure, composition and antibacterial assay. Mater Sci Eng C 2019;97:420—30. https://doi.org/10.1016/j.msec.2018.12.045.

[26] Jaafar A, Hecker C, Árki P, Joseph Y. Sol-gel derived hydroxyapatite coatings for titanium implants: a review. Bioengineering 2020;7:1—23. https://doi.org/10.3390/bioengineering7040127.

[27] Priyadarshini B, Ramya S, Shinyjoy E, Kavitha L, Gopi D, Vijayalakshmi U. Structural, morphological and biological evaluations of cerium incorporated hydroxyapatite sol-gel coatings on Ti-6Al-4V for orthopaedic applications. J Mater Res Technol 2021;12:1319—38. https://doi.org/10.1016/j.jmrt.2021.03.009.

[28] Coelho MFC, Sousa LL, Ferreira CC, Souza BFG, Rigo EC da S, Mariano NA. Biomimetic coating on titanium: evaluation of bioactivity and corrosion. Mater Res Express 2020;6:1265g5. https://doi.org/10.1088/2053-1591/ab67f1.

[29] Stevanović M, Djošić M, Janković A, Kojić V, Vukašinović-Sekulić M, Stojanović J, et al. Antibacterial graphene-based hydroxyapatite/chitosan coating with gentamicin for potential applications in bone tissue engineering. J Biomed Mater Res Part A 2020:1—15. https://doi.org/10.1002/jbm.a.36974.

[30] Stevanović M, Ðošić M, Janković A, Kojić V, Vukašinović-Sekulić M, Stojanović J, et al. Gentamicin-loaded bioactive hydroxyapatite/chitosan composite coating electrodeposited on titanium. ACS Biomater Sci Eng 2018;4:3994—4007. https://doi.org/10.1021/acsbiomaterials.8b00859.

[31] Djošić M, Janković A, Mišković-Stanković V. Electrophoretic deposition of biocompatible and bioactive hydroxyapatite-based coatings on titanium. Materials (Basel) 2021;14:5391. https://doi.org/10.3390/ma14185391.

[32] Gunawarman, Nuswantoro NF, Juliadmi D, Fajri H, Budiman A, Tjong DH, et al. Hydroxyapatite coatings on titanium alloy TNTZ using electrophoretic deposition. IOP Conf Ser Mater Sci Eng 2019;602:012071. https://doi.org/10.1088/1757-899X/602/1/012071.

[33] Bakhshandeh S, Amin Yavari S. Electrophoretic deposition: a versatile tool against biomaterial associated infections. J Mater Chem B 2018;6:1128—48. https://doi.org/10.1039/c7tb02445b.

[34] Kattimani VS, Kondaka S, Lingamaneni KP. Hydroxyapatite—-past, present, and future in bone regeneration. Bone Tissue Regen Insights 2016;7:BTRI.S36138. https://doi.org/10.4137/btri.s36138.

[35] Awasthi S, Pandey SK, Arunan E, Srivastava C. A review on hydroxyapatite coatings for the biomedical applications: experimental and theoretical perspectives. J Mater Chem B 2021;9:228—49. https://doi.org/10.1039/d0tb02407d.

[36] Zielinski A, Bartmanski M. Electrodeposited biocoatings, their properties and fabrication technologies: a review 2020;10. https://doi.org/10.3390/COATINGS10080782.

[37] Sultankulov B, Berillo D, Sultankulova K, Tokay T, Saparov A. Progress in the development of chitosan-based biomaterials for tissue engineering and regenerative medicine. Biomolecules 2019;9. https://doi.org/10.3390/biom9090470.

[38] Parhi R. Drug delivery applications of chitin and chitosan: a review. Environ Chem Lett 2020;18:577—94. https://doi.org/10.1007/s10311-020-00963-5.

[39] Stevanović M, Djošić M, Janković A, Rhee KY, Mišković-Stanković V. Electrophoretically deposited hydroxyapatite-based composite coatings loaded with silver and gentamicin as antibacterial agents. J Serbian Chem Soc 2019;84:1287—304. https://doi.org/10.2298/JSC190821092S.

[40] Herdiana Y, Wathoni N, Shamsuddin S, Joni IM, Muchtaridi M. Chitosan-based nanoparticles of targeted drug delivery system in breast cancer treatment. 2021.

[41] Boudemagh D, Venturini P, Fleutot S, Cleymand F. Elaboration of hydroxyapatite nanoparticles and chitosan/hydroxyapatite composites: a present status. Springer Berlin Heidelberg 2019;76. https://doi.org/10.1007/s00289-018-2483-y.

[42] Karimi N, Kharaziha M, Raeissi K. Electrophoretic deposition of chitosan reinforced graphene oxide-hydroxyapatite on the anodized titanium to improve biological and electrochemical characteristics. Mater Sci Eng C 2019;98. https://doi.org/10.1016/j.msec.2018.12.136.

[43] Said HA, Noukrati H, Youcef H Ben, Bayoussef A, Oudadesse H, Barroug A. Mechanical behavior of hydroxyapatite-chitosan composite: effect of processing parameters. Minerals 2021;11:1–10. https://doi.org/10.3390/min11020213.

[44] Li B, Xia X, Guo M, Jiang Y, Li Y, Zhang Z, et al. Biological and antibacterial properties of the micro-nanostructured hydroxyapatite/chitosan coating on titanium. Sci Rep 2019;9:1–10. https://doi.org/10.1038/s41598-019-49941-0.

[45] Hoseini-Ghahfarokhi M, Mirkiani S, Mozaffari N, Abdolahi Sadatlu MA, Ghasemi A, Abbaspour S, et al. Applications of graphene and graphene oxide in smart drug/gene delivery: is the world still flat? Int J Nanomedicine 2020;15:9469–96. https://doi.org/10.2147/IJN.S265876.

[46] Fardi SR, khorsand H, Askarnia R, Pardehkhorram R, Adabifiroozjaei E. Improvement of biomedical functionality of titanium by ultrasound-assisted electrophoretic deposition of hydroxyapatite-graphene oxide nanocomposites. Ceram Int 2020;46:18297–307. https://doi.org/10.1016/j.ceramint.2020.05.049.

[47] Ballarre J, Aydemir T, Liverani L, Roether JA, Goldmann WH, Boccaccini AR. Versatile bioactive and antibacterial coating system based on silica, gentamicin, and chitosan: improving early stage performance of titanium implants. Surf Coat Technol 2020;381. https://doi.org/10.1016/j.surfcoat.2019.125138.

[48] Aydemir T, Liverani L, Pastore JI, Ceré SM, Goldmann WH, Boccaccini AR, et al. Functional behavior of chitosan/gelatin/silica-gentamicin coatings by electrophoretic deposition on surgical grade stainless steel. Mater Sci Eng C 2020;115:111062. https://doi.org/10.1016/j.msec.2020.111062.

[49] Stevanović M, Djošić M, Janković A, Nešović K, Kojić V, Stojanović J, et al. Assessing the bioactivity of gentamicin-preloaded hydroxyapatite/chitosan composite coating on titanium substrate. ACS Omega 2020;5:15433–45. https://doi.org/10.1021/acsomega.0c01583.

[50] Kokubo T, Takadama H. How useful is SBF in predicting in vivo bone bioactivity? Biomaterials 2006;27:2907–15. https://doi.org/10.1016/j.biomaterials.2006.01.017.

[51] Abcam. Alkaline phosphatase assay kit. Abcam 2015;1:1–11.

[52] Chen Y, Feng Y, Deveaux JG, Masoud MA, Chandra FS, Chen H, et al. Biomineralization forming process and bio-inspired nanomaterials for biomedical application: a review. Minerals 2019;9:68. https://doi.org/10.3390/min9020068.

[53] Zhang Q, Leng Y, Lu X, Xin R, Yang X, Chen J. Bioactive films on metallic surfaces for osteoconduction. J Biomed Mater Res Part A 2009;88:481–90. https://doi.org/10.1002/jbm.a.31820.

[54] Leeuwenburgh SCG, Wolke JGC, Siebers MC, Schoonman J, Jansen JA. In vitro and in vivo reactivity of porous, electrosprayed calcium phosphate coatings. Biomaterials 2006;27:3368–78. https://doi.org/10.1016/j.biomaterials.2006.01.052.

[55] Zadpoor AA. Relationship between in vitro apatite-forming ability measured using simulated body fluid and in vivo bioactivity of biomaterials. Mater Sci Eng C 2014;35:134–43. https://doi.org/10.1016/j.msec.2013.10.026.

[56] Murugan N, Murugan C, Sundramoorthy AK. In vitro and in vivo characterization of mineralized hydroxyapatite/polycaprolactone-graphene oxide based bioactive multifunctional coating on Ti alloy for bone implant applications. Arab J Chem 2018;11:959–69. https://doi.org/10.1016/j.arabjc.2018.03.020.

[57] Mohammad Salahi Tohidi P, Safavi MS, Etminanfar M, Khalil-Allafi J. Pulsed electrodeposition of compact, corrosion resistant, and bioactive HAp coatings by application of optimized magnetic field. Mater Chem Phys 2020;254:123511. https://doi.org/10.1016/j.matchemphys.2020.123511.

[58] Berzina-Cimdina L, Borodajenko N. Research of calcium phosphates using Fourier transform infrared spectroscopy. Infrared Spectrosc Mater Sci Eng Technol 2012:123–48. https://doi.org/10.5772/36942.

[59] Cromme P, Zollfrank C, Müller L, Müller FA, Greil P. Biomimetic mineralisation of apatites on Ca2+ activated cellulose templates. Mater Sci Eng C 2007;27:1–7. https://doi.org/10.1016/j.msec.2005.11.001.

[60] Ren F, Ding Y, Leng Y. Infrared spectroscopic characterization of carbonated apatite: a combined experimental and computational study. J Biomed Mater Res Part A 2014;102:496–505. https://doi.org/10.1002/jbm.a.34720.

[61] Bonadio TGM, Sato F, Medina AN, Weinand WR, Baesso ML, Lima WM. Bioactivity and structural properties of nanostructured bulk composites containing Nb2O5 and natural hydroxyapatite. J Appl Phys 2013;113. https://doi.org/10.1063/1.4809653.

[62] Barinov SM, Rau JV, Cesaro SN, Ďurišin J, Fadeeva IV, Ferro D, et al. Carbonate release from carbonated hydroxyapatite in the wide temperature rage. J Mater Sci Mater Med 2006;17:597–604. https://doi.org/10.1007/s10856-006-9221-y.

[63] Madupalli H, Pavan B, Tecklenburg MMJ. Carbonate substitution in the mineral component of bone: discriminating the structural changes, simultaneously imposed by carbonate in A and B sites of apatite. J Solid State Chem 2017;255:27–35. https://doi.org/10.1016/j.jssc.2017.07.025.

[64] Peng F, Veilleux E, Schmidt M, Wei M. Synthesis of hydroxyapatite nanoparticles with tailorable morphologies and carbonate substitutions using a wet precipitation method. J Nanosci Nanotechnol 2012;12:2774–82. https://doi.org/10.1166/jnn.2012.5714.

[65] Yang W, Xi X, Li J, Cai K. Comparison of crystal structure between carbonated hydroxyapatite and natural bone apatite with theoretical calculation. Asian J Chem 2013;25:3673–8.

[66] Rincón-López JA, Hermann-Muñoz JA, Giraldo-Betancur AL, De Vizcaya-Ruiz A, Alvarado-Orozco JM, Muñoz-Saldaña J. Synthetic and bovine-derived hydroxyapatite ceramics: a comparison. Materials (Basel) 2018;11:17. https://doi.org/10.3390/ma11020333.

[67] Sarma BK, Barman P, Sarma B, Das A, Pal AR. Biomimetic deposition of carbonate apatite and role of carbonate substitution on mechanical properties at nanoscale. Mater Lett 2016;185:387–90. https://doi.org/10.1016/j.matlet.2016.09.028.

[68] Sakthivel P, Ragu A, Senthilarasan K. Synthesis and characterization of hydroxyapatite with tamarind kernel powder (bio-polymer) for biomedical applications. Int J Eng Sci Res Technol 2015;4:631–5.

[69] Chen X, Wu D, Xu J, Yan T, Chen Q. Gelatin/Gelatin-modified nano hydroxyapatite composite scaffolds with hollow channel arrays prepared by extrusion molding for bone tissue engineering. Mater Res Express 2021;8. https://doi.org/10.1088/2053-1591/abde1f.

[70] Ishikawa K, Ducheyne P, Radin S. Determination of the Ca/P ratio in calcium-deficient hydroxyapatite using X-ray diffraction analysis. J Mater Sci Mater Med 1993;4:165–8. https://doi.org/10.1007/BF00120386.

[71] Wopenka B, Pasteris JD. A mineralogical perspective on the apatite in bone. Mater Sci Eng C 2005;25:131–43. https://doi.org/10.1016/j.msec.2005.01.008.

[72] Bonfield W, Gibson IR. Novel synthesis and characterization of an AB-type carbonate-substituted hydroxyapatite. J Biomed Mater Res 2002;59:697–708. https://doi.org/10.1002/jbm.10044.

[73] Cacciotti I. Cationic and anionic substitutions in hydroxyapatite. In: Antoniac IV, editor. Handb. Bioceram. Biocomposites. Switzerland: Springer International Publishing; 2016. p. 146–88. https://doi.org/10.1007/978-3-319-12460-5_7.

[74] Borkowski L, Sroka-Bartnicka A, Draczkowski P, Ptak A, Zięba E, lósarczyk A, et al. The comparison study of bioactivity between composites containing synthetic non-substituted and carbonate-substituted hydroxyapatite. Mater Sci Eng C 2016;62:260—7. https://doi.org/10.1016/j.msec.2016.01.056.

[75] Djošić MS, Mitrić M, Mišković-Stankovic VB. The porosity and roughness of electrodeposited calcium phosphate coatings in simulated body fluid. J Serbian Chem Soc 2015;80:237—51. https://doi.org/10.2298/JSC140626098D.

[76] Zhang Q, Chen J, Feng J, Cao Y, Deng C, Zhang X. Dissolution and mineralization behaviors of HA coatings. Biomaterials 2003;24:4741—8. https://doi.org/10.1016/S0142-9612(03)00371-5.

[77] Kumar M, Dasarathy H, Riley C. Electrodeposition of brushite coatings and their transformation to hydroxyapatite in aqueous solutions. J Biomed Mater Res 1999;45:302—10. https://doi.org/10.1002/(SICI)1097-4636(19990615)45:4<302::AID-JBM4>3.0.CO;2-A.

[78] Sun R, Chen K, Lu Y. Fabrication and dissolution behavior of hollow hydroxyapatite microspheres intended for controlled drug release. Mater Res Bull 2009;44:1939—42. https://doi.org/10.1016/j.materresbull.2009.06.015.

[79] Hsu CH, Mansfeld F. Concerning the conversion of the constant phase element parameter Y0 into a capacitance. Corrosion 2001;57:747—8. https://doi.org/10.5006/1.3280607.

[80] Permyakova ES, Manakhov AM, Kiryukhantsev-Korneev PV, Sheveyko AN, Gudz KY, Kovalskii AM, et al. Different concepts for creating antibacterial yet biocompatible surfaces: adding bactericidal element, grafting therapeutic agent through COOH plasma polymer and their combination. Appl Surf Sci 2021;556:149751. https://doi.org/10.1016/j.apsusc.2021.149751.

[81] Korsmeyer RW, Gurny R, Doelker E, Buri P, Peppas NA. Mechanisms of solute release from porous hydrophilic polymers. Int J Pharm 1983;15:25—35. https://doi.org/10.1016/0378-5173(83)90064-9.

[82] Ritger PL, Peppas NA. A simple equation for description of solute release. J Control Release 1987;5:23—36.

[83] Pandey H, Parashar V, Parashar R, Prakash R, Ramteke PW, Pandey AC. Controlled drug release characteristics and enhanced antibacterial effect of graphene nanosheets containing gentamicin sulfate. Nanoscale 2011;3:4104—8. https://doi.org/10.1039/c1nr10661a.

[84] Goenka S, Sant V, Sant S. Graphene-based nanomaterials for drug delivery and tissue engineering. J Control Release 2014;173:75—88. https://doi.org/10.1016/j.jconrel.2013.10.017.

[85] Liu J, Dong J, Zhang T, Peng Q. Graphene-based nanomaterials and their potentials in advanced drug delivery and cancer therapy. J Control Release 2018;286:64—73. https://doi.org/10.1016/j.jconrel.2018.07.034.

[86] Yoshizawa S. Structural origins of gentamicin antibiotic action. EMBO J 1998;17:6437—48. https://doi.org/10.1093/emboj/17.22.6437.

[87] Vimalraj S. Alkaline phosphatase: structure, expression and its function in bone mineralization. Gene 2020;754:144855. https://doi.org/10.1016/j.gene.2020.144855.

[88] Beertsen W, Van den Bos T. Alkaline phosphatase induces the mineralization of sheets of collagen implanted subcutaneously in the rat. J Clin Invest 1992;89:1974—80. https://doi.org/10.1172/JCI115805.